tvst

Article

Software for Quantifying and Batch Processing Images of Brn3a and RBPMS Immunolabelled Retinal Ganglion Cells in Retinal Wholemounts

Chelsea Guymer[1], Lloyd Damp[2], Glyn Chidlow[1], John Wood[1], Yi Fan Tang[3], and Robert Casson[1,3]

[1] Ophthalmic Research Laboratories, Discipline of Ophthalmology and Visual Sciences, University of Adelaide, Adelaide Health and Medical Sciences Building, North Terrace, Adelaide, Australia
[2] Southern Launch, Adelaide, Australia
[3] Department of Ophthalmology, Royal Adelaide Hospital, Adelaide, Australia

Correspondence: Robert Casson, Ophthalmic Research Laboratories, Level 7 Adelaide Health and Medical Sciences Building, The University of Adelaide, North Terrace, Adelaide SA 5000, Australia. e-mail: robert.casson@adelaide.edu.au

Received: September 6, 2019
Accepted: April 1, 2020
Published: May 27, 2020

Keywords: retinal ganglion cell; quantification; software; retinal wholemount; batch processing

Citation: Guymer C, Damp L, Chidlow G, Wood J, Tang YF, Casson R. Software for quantifying and batch processing images of Brn3a and RBPMS immunolabelled retinal ganglion cells in retinal wholemounts. Trans Vis Sci Tech. 2020;9(6):28, https://doi.org/10.1167/tvst.9.6.28

Purpose: The ability to accurately quantify immunohistochemically labeled retinal ganglion cells (RGCs) on wholemounts is an important histopathological determinant in experimental retinal research. Traditionally, this has been performed by manual or semi-automated counting of RGCs. Here, we describe an automated software that accurately and efficiently counts immunolabeled RGCs with the ability to batch process images and perform whole-retinal analysis to permit isodensity map generation.

Methods: Retinal wholemounts from control rat eyes, and eyes subjected to either chronic ocular hypertension or N-methyl-D-aspartate (NMDA)-induced excitotoxicity, were labeled by immunohistochemistry for two different RGC-specific markers, Brn3a and RNA-binding protein with multiple splicing (RBPMS). For feasibility of manual counting, images were sampled from predefined retinal sectors, totaling 160 images for Brn3a and 144 images for RBPMS. The automated program was initially calibrated for each antibody prior to batch analysis to ensure adequate cell capture. Blinded manual RGC counts were performed by three independent observers.

Results: The automated counts of RGCs labeled for Brn3a and RBPMS closely matched manual counts. The automated script accurately quantified both physiological and damaged retinas. Efficiency in counting labeled RGC wholemount images is accelerated 40-fold with the automated software. Whole-retinal analysis was demonstrated with integrated retinal isodensity map generation.

Conclusions: This automated cell counting software dramatically accelerates data acquisition while maintaining accurate RGC counts across different immunolabels, methods of injury, and spatial heterogeneity of RGC loss. This software likely has potential for wider application.

Translational Relevance: This study provides a valuable tool for preclinical RGC neuroprotection studies that facilitates the translation of neuroprotection to the clinic.

Introduction

Glaucoma describes a group of ocular conditions united by a clinically characteristic intraocular pressure (IOP)-associated optic neuropathy with associated loss of retinal ganglion cells (RGCs).[1] Currently, IOP reduction is the only proven treatment; however, additional neuroprotective strategies that attenuate RGC loss would be highly clinically desirable.

Quantification of RGCs on retinal wholemounts is a commonly used outcome measure in preclinical

studies investigating potential efficacy of neuroprotectants to RGCs in animal models. A variety of labeling techniques can be used to assess RGC survival, including the use of retrograde tracers, such as Fluorogold; labeling with neuronal markers, such as NeuN, Neurotrace, or βIII-tubulin; or immunolabeling with RGC specific markers, including Brn3a, RNA-binding protein with multiple splicing (RBPMS), and gamma (γ)-synuclein.[2–16] Each marker provides a different methodological challenge. For example, quantifying RGCs using markers, such as γ-synuclein, that stain axons as well as somas is problematic from a technical perspective, because labeled axon fibers often obscure underlying RGCs.[7]

RGC quantification is typically approached by selectively imaging predefined sectoral regions of the retina at set distances from the optic nerve and counting the number of RGCs within each region.[14] Semi-automated or manual counting methods are normally used, and these are labor-intensive, time-consuming, and open to subjective bias. Sectoral differences in RGC density can also produce bias in the results, unless the entire retina is imaged.[17] Rapid automation of RGC quantification on retinal wholemounts, therefore, has the potential to accelerate data collection and reduce bias. It could also potentially be applied to the whole retina, enabling the generation of RGC isodensity maps.[10,16]

A limited variety of software packages have been developed to expedite cell counting in rodent retinal wholemounts. These include commercially available software, such as MetaMorph,[18] StereoInvestigator,[19] and IPlab;[20] novel programs created by individual laboratories[10,21]; and open-source programs, such as ImageJ and CellProfiler, with macros providing automated cell counting functionality (see Table 4). However, the wider adoption of these programs has been limited, perhaps due to the limited applicability to different immunolabels or tissue mediums.

Here, we present an automated, freely available software validated for RGC-specific labels Brn3a and RBPMS in rodent retinal wholemounts. It has the capacity to differentiate individual cells in a cluster, batch process images with the same immunolabel, and export the results in tabular format to a spreadsheet to expedite data analysis. This program has been validated on RGC-specific immunolabels on confocal low magnification ($\times$10) images, can tolerate both naïve and injured retina interchangeably, and has the added feature of automatically subtracting dirt or artifacts in the case of imperfect immunostaining. It also has the ability to provide whole-retinal analysis and integrated retinal isodensity map generation.

Materials and Methods

Animals and Procedures

This project was approved by the Animal Ethics Committees of SA Pathology/Central Adelaide Local Health Network and the University of Adelaide (Adelaide, Australia) and conformed with the Australian Code of Practice for the Care and Use of Animals for Scientific Purposes, 2013, and with the ARVO Statement for the use of animals in vision and ophthalmic research. Adult Sprague-Dawley rats (aged 10 weeks+, <230 g; $n = 18$) were housed in a temperature- and humidity-controlled room with 12-hour light and dark cycles. Food and water were provided ad libitum.

The experimental plan comprised three cohorts of animals (groups 1 to 3) that were immunolabeled and analyzed as discrete batches. For group 1, experimental glaucoma was induced in the right eye, leaving the untouched left eye to serve as a control. This group comprised $n = 10$ injured eyes and $n = 10$ naïve eyes and all eyes were analyzed for Brn3a. Glaucoma was induced using a slightly modified protocol of the method described by Levkovitch-Verbin et al.[22] Rats were humanely euthanized after two weeks. Elevated IOP over the course of two weeks using this model causes measurable loss of RGCs and their axons.[23,24] Group 2 comprised $n = 4$ untreated rats of which one eye per rat was analyzed for RBPMS. For group 3, an intravitreal injection of 40 nmol of NMDA (5 µl in sterile saline) was performed in the right eye, leaving the untouched left eye to serve as a control. Group 3 comprised $n = 4$ injured eyes and $n = 4$ naïve eyes and all eyes were analyzed for RBPMS. Rats were humanely euthanized after one week, because NMDA causes a marked loss of RGCs at this time point.[25,26]

Tissue Processing and Immunohistochemistry

All rats were terminally anesthetized by transcardial perfusion using physiological saline. Whole eyes were removed and placed in 10% neutral buffered formalin for one hour. Posterior eye-cups were carefully dissected and each retina was prepared as a flattened wholemount via four relaxing incisions. Retinas were permeabilized with phosphate buffered saline (PBS; 137 mM NaCl, 5.4 mM KCl, 1.28 mM NaH_2PO_4, 7 mM Na_2HPO_4; and pH 7.4) containing 1% Triton X-100 (PBST-1%), blocked in PBST-1% containing 3% (v/v) normal horse serum, then incubated for three days at 4°C in the same solution containing either goat

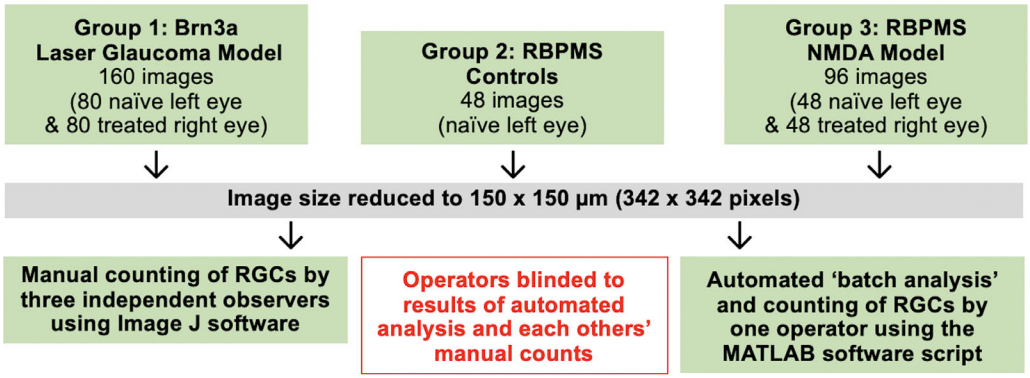

Figure 1. Flowchart summarizing the protocol followed for manual and automated analysis of immunolabeled images.

anti-Brn3a primary antibody (1:600; SC-31984; Santa Cruz Biotechnology, Santa Cruz, CA) or rabbit anti-RBPMS primary antibody (1:500; ABN1362; Merck Millipore, Bayswater, Victoria, Australia).

After multiple washes with PBST, wholemounts were incubated overnight at 4˚C with alexa fluor 488 or 594-conjugated donkey anti-goat secondary antibody (for Brn3a) or alexa fluor 488 or 594-conjugated donkey anti-rabbit secondary antibody (for RBPMS; 1:500; Invitrogen, Mulgrave, Victoria, Australia), before rinsing in PBS and mounting using anti-fade mounting medium.

Imaging of Retinal Wholemounts

Wholemounts were examined under a confocal microscope with images captured at 10× magnification, corresponding to a sampling region of 700 × 525 µm. For feasibility of manual counting, of this sampled region the image was cropped to 150 × 150 µm and these fames were manually and automatically quantified. For Brn3a (group 1), images were sampled from both central and peripheral regions of each of the superior, inferior, nasal, and temporal quadrants, corresponding to eight images per sampled retina. For RBPMS (groups 2 and 3), images were sampled from central, middle, and peripheral regions of each superior, inferior, nasal, and temporal quadrants, corresponding to 12 images per sampled retina (Fig. 1). The primary aim of this study was to compare the accuracy of manual counts to corresponding automated cell counts in each sampled image for each immunolabel rather than measuring the effect of any intervention on RGC density. Therefore, the manual cell count was directly compared with the corresponding automated cell count of each immunolabeled image and results collated for each RGC marker.

To demonstrate RGC quantification of entire retinal wholemounts with corresponding retinal isodensity map generation, high resolution images of two naïve entire retinal wholemounts immunolabelled with Brn3a were captured on Hamamatsu NanoZoomer 2.0-HT fluorescence module at 20× magnification. These images were viewed using the Hamamatsu NanoZoomer Digital Pathology system and exported as a TIFF.

Algorithm Development

The code steps through five procedures that "de-clump" and count "circular" cells within an image. The first three steps are designed to intensify the boundary between cells. Existing programs can count cells when the images are well structured with clear boundaries between cells but are often compromised by: (1) cell clumping or overlapping; (2) nonuniform illumination; (3) artifacts; (4) markers camouflaged by background noise; and (5) irregularity of shape.

The fourth step undertakes an analysis of the prepared image and identifies areas of circular patterns using an efficient Hough transform. An optional fifth step checks the validity of the cell count generated in the fourth step by comparing the integrated image intensity within the proposed cell to a user specified threshold, the degree to which the cell is filled as well as the overlap between neighboring cells. An optional heat map can be generated from the output from steps 4 and 5 based on the industry standard Kernel Density Function using a gaussian Kernel. Please refer to Supplementary Material S1 for a more detailed explanation of the algorithm development. A graphic user interface (GUI) for the algorithm was developed to facilitate ease of use, with an example and explanation of its functions demonstrated in Figure 2.

Batch Processing

The user has the option to batch-process a directory of images using either a set of parameters

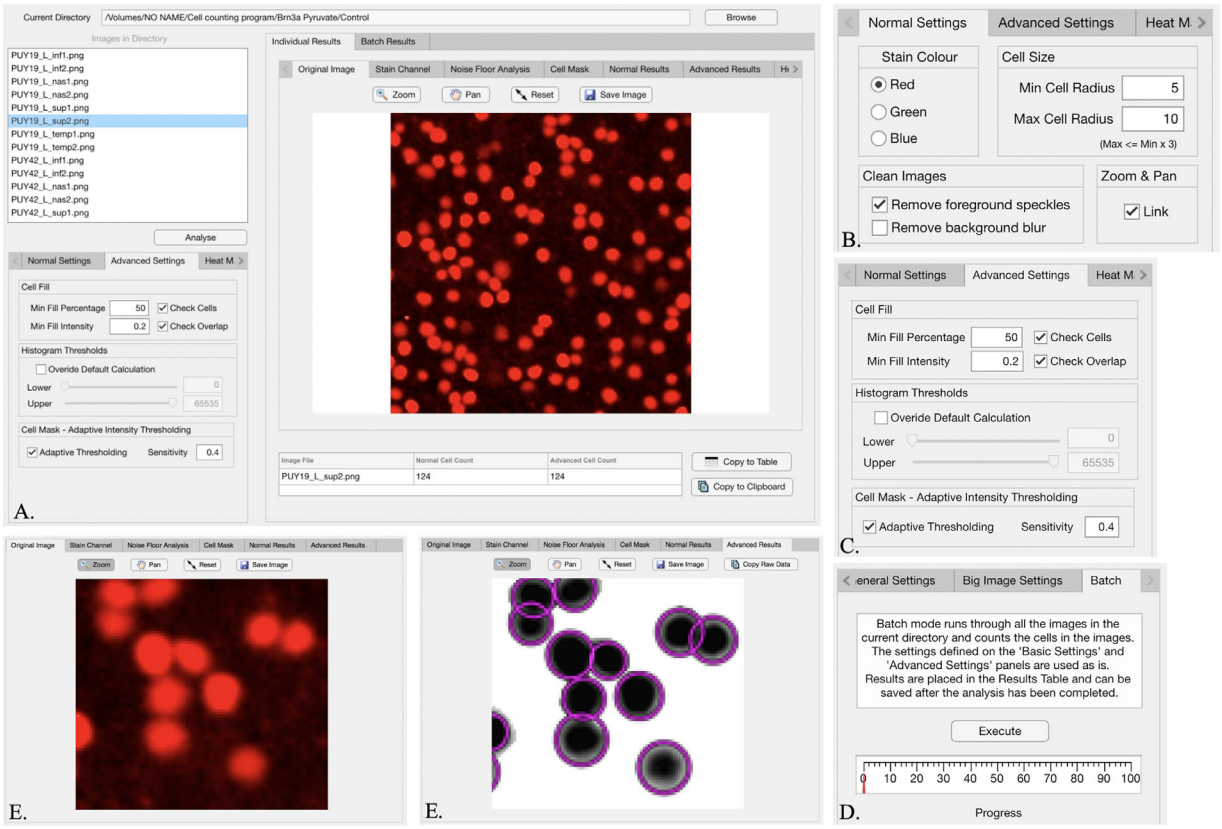

Figure 2. Interface of the Automated Cell Counting Program Software. (A) The "browse" option allows the user to access image folders and files, as listed in the upper left window titled "Images in Directory." (B, C) Images can be individually analyzed with user-defined parameters calibrated to accurately capture and quantify cells, or (D) a "batch" analysis can be performed of all images in that directory using the highlighted tab in the bottom left window. In this window, the user can select the settings necessary to direct automated cell capture and quantification by the algorithm, such as (B) stain color, cell size (setting the radius of the circular sample, which defines the immunolabeled cell), "clean images" option to remove foreground speckles (i.e. artifact) or background blur (background noise), (C) "cell fill" defining the minimum threshold by which the immunolabel should occupy the circular sample (expressed as a percentage), and minimal fill intensity (i.e. brightness / intensity of stain color taken up by the cell). The "check cell" option will circumscribe the cells identified by these parameters in the "advanced results" tab to allow the user to check automated cell capture against the original image. The "normal results" tab circumscribes cells based on all user-defined parameters other than the "cell fill" and "minimal fill intensity" options. (B, E) The "link zoom" feature allows a zoomed-in area of interest from the original image to be mirrored in the "normal results" and "advanced results" tabs to allow the user to manually check the accuracy of automated cell capture and adjust the settings to optimize the result. Tabulated results can be exported to Excel for ease of data analysis.

determined in advance by the user or by letting the program automatically threshold a number of images stored together using the above method. Processed images are annotated to indicate the number of cells counted, along with the estimated cell boundaries. Results are provided in tabular format for further statistical analysis with user controls simplifying the data export to comma separated value (CSV) format.

Data Acquisition

The program was initially calibrated for each respective immunohistochemical label prior to batch analysis (i.e. all images of that label were seamlessly analyzed using the same objective parameters set by the user to ensure adequate cell capture). Calibrations taken into account were as follows: (1) stain color channel (red, green, and blue), (2) cell size (pixels), (3) option to remove foreground speckles (artifact) or background blur for imperfect immunostaining, (4) cell fill (i.e. the minimum fill percentage was set to 50%, indicating that for cells abutting the border of an image at least 50% of its sphere must be visible for it to be counted, and minimum fill intensity was set to 0.2 (20%), to exclude background artifact and poorly visible background cells without clear border definition), and (5) adaptive

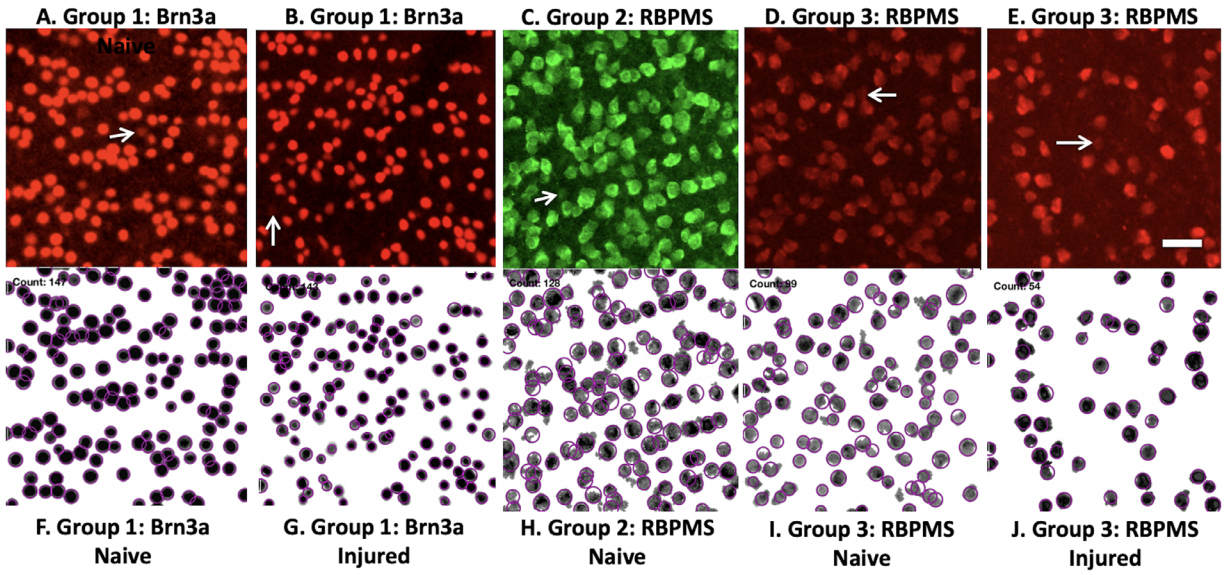

Figure 3. Representative immunolabeled images for Brn3a and RBPMS (A–E) and the corresponding processed images ready for automated counting (F–J). Scale bar = 25 µm, 10 × magnification immunolabeled confocal photomicrographs, 150 × 150 µm cropped frames. Arrows demonstrate faintly visible cells in the background with poor border definition, which were excluded from both manual and automated counts.

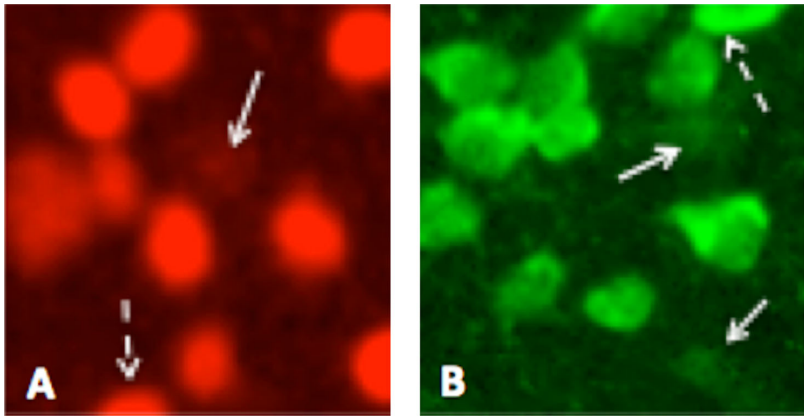

Figure 4. Examples of counting rules followed by manual observers (please note zoomed-in images are not to scale). (A) Brn3a immunolabelled RGCs. (B) RBPMS immunolabelled RGCs. Arrows (→) highlight faintly visible cells with poor border definition and dashed arrows; (–>) demarcate cells of which <50% of the cell was visualized on the image border, both of which were excluded from manual counts.

thresholding of 0.4 that calculates a locally adaptive lighting threshold with a sensitivity toward thresholding more pixels as background than foreground. These parameters were in keeping with manual "counting rules," as described below. Apart from being aware of which particular label was being quantified, automated analyses were performed in a blinded fashion (i.e. the operator remained unaware of the corresponding manual count for each image). An example of the end point of processing to produce automated counts of RGCs for each particular label and group is shown in Figure 3.

Manual RGC counts were acquired by three independent observers using the "point tool" counter with ImageJ software (imagej.net, version 2.0.0-rc-43/1.51q). Observers were provided with "counting rules" to follow, namely: (1) cells that were abutting the boundary of the image were only to be counted if at least 50% of the cell was visualized (i.e. forming a semicircle, but no less), and (2) poorly visible cells in the background were to be excluded if their cell boundaries were not clearly evident (Fig. 4). Observers were blinded both to counts from other observers and to that of the automated cell counting software.

Table 1. ICC (95% CI) of Immunohistochemical Labels (Correlation Between all Three Observers)

	Group 1: Brn3a (OHT model)	Group 2: RBPMS (Controls only)	Group 3: RBPMS (NMDA model)
Naïve retina	0.876 (0.826 to 0.914)	0.924 (0.882 to 0.954)	0.977 (0.964 to 0.986)
Injured retina	0.991 (0.987 to 0.994)	N/A	0.917 (0.871 to 0.950)

CI, confidence interval; ICC, intraclass correlation coefficient; N/A, not applicable; NMDA, *N*-methyl-D-aspartate; OHT, ocular hypertension.

Table 2. Bland-Altman Tests - Bias (95% Limits of Agreement) (GT versus Automated Counts)

	Group 1: Brn3a (OHT model)	Group 2: RBPMS (Controls only)	Group 3: RBPMS (NMDA model)
Naïve retina	−0.231 (−7.209 to 6.747)	−0.314 (−12.054 to 11.426)	−0.058 (−12.130 to 12.014)
Injured retina	−3.03 (−18.553 to 12.493)	N/A	5.18 (−4.700 to 15.060)

GT, ground truth (average of manual counts of three independent observers); NMDA, *N*-methyl-D-aspartate; N/A, not applicable; OHT, ocular hypertension.

Table 3. Linear Regression Analysis – Slope of Best Fit (R2) (GT vs Automated Counts)

	Group 1: Brn3a (OHT model)	Group 2: RBPMS (Controls only)	Group 3: RBPMS (NMDA model)
Naïve retina	0.909 (0.979)	0.801 (0.875)	0.962 (0.979)
Injured retina	0.949 (0.991)	N/A	0.945 (0.978)

GT, ground truth (average of manual counts of three independent observers); NMDA, *N*-methyl-D-aspartate; N/A, not applicable; OHT, ocular hypertension.

Results

The average manual count of the three independent observers was set as the ground truth (GT). Agreement among the observers was quantified using the intraclass correlation coefficient (ICC; Table 1). Agreement between the GT and the automated cell count was investigated using Bland-Altman plots (Table 2, Fig. 5), and linear regression analysis (R2; Table 3, Fig. 6) was used to model the relationship between these two variables. To obtain accurate estimates of the SDs in the Bland-Altman plots, which accounted for the correlated nature of the data (multiple images from each rat retina), a linear mixed model was constructed and the variance components analyzed.[27,28] Statistical analyses were performed by using statistical software GraphPad Prism 8 and R statistical Software. Integrated whole retinal analysis and retinal isodensity map generation are demonstrated (Fig. 7).

Overall Performance of Automated versus Manual Counts on Brn3a and RBPMS Immunolabeled Retina

There was excellent agreement among the three experienced observers performing the manual cell counts (Table 1) and the automated script performed equally well for both healthy and damaged retinas (Table 2, Table 3, Fig. 5, Fig. 6). Each immunolabeled image took a manual observer approximately 2 minutes to count, whereas the automated program was able to batch process 40 immunolabelled images within 2 minutes. Hence, efficiency in counting immunolabeled

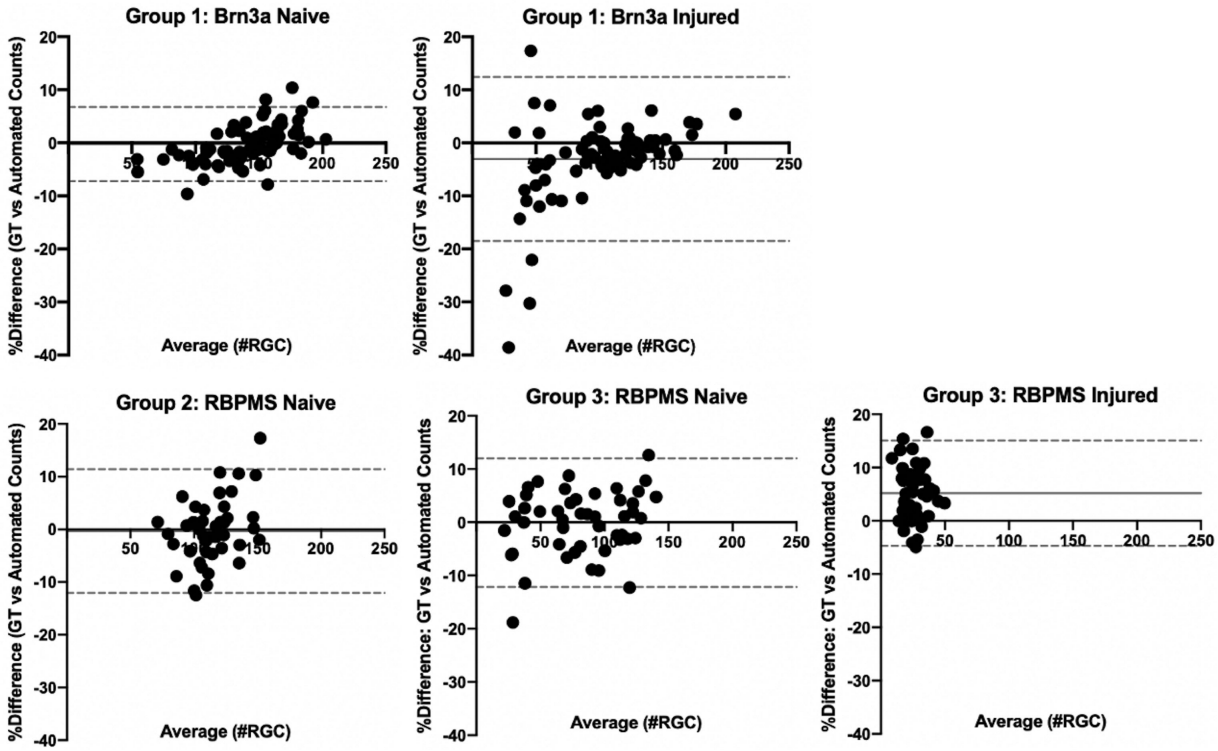

Figure 5. Bland-Altman Plots of Ground Truth (GT) versus Automated Counts in both naive and injured retina. The uninterrupted line (___) indicates the bias. The dashed lines (—) indicate the 95% limits of agreement. Group 1, Brn3a OHT model ($n = 80$ frames for both naïve and injured retinas); group 2, RBPMS naïve cohort ($n = 48$ frames for naïve retinas only); group 3, RBPMS NMDA model ($n = 48$ frames for both naïve and injured retinas).

RGC wholemount images can be accelerated by 40-fold using the automated script.

Bland-Altman tests (Table 2, Fig. 5) in Brn3a and RBPMS immunolabeled retinal images taken from naïve retina across all groups (1-3) calculated a bias close to zero (−0.314 to −0.058). This indicates that, on average, there was almost no difference between manual and automated counts. There was more ambiguity in the average difference in manual and automated counts for group 1 Brn3a immunolabeled injured retinal images and group 3 RBPMS immunolabeled injured retinal images, given the larger bias (−3.03 and 5.18, respectively) and 95% limits of agreement (−18.553 to 12.493, and −4.700 to 15.060, respectively). The quality of immunohistochemistry was varied both within and between sampled groups, for naïve and injured retina, and the quality of immunohistochemistry labeling can influence the accuracy of the automated cell counts. Injured retinas generally exhibited poorer quality immunolabeling, with increased background staining and artifact, which may account for the difference.

Linear regression analysis (Table 4, Fig. 6) of automated versus manual counting for group 1 (ocular hypertension model) Brn3a-labeled RGCs demonstrated a slope of best fit of 0.909 (naïve retina) and 0.949 (injured retina) with R2 of 0.979 and 0.991, respectively. Similarly, group 3 (NMDA model) RBPMS-labeled RGCs demonstrated a slope of best fit of 0.962 (naïve retina) and 0.945 (injured retina) with R2 of 0.979 and 0.978, respectively. Given that the slope was almost 1, this indicates that essentially no underestimation occurred. For group 2 naïve RBPMS-labeled RGCs, linear regression analysis of automated versus manual counting demonstrated a slope of best linear fit of 0.801 with R2 of 0.875, indicating a slight underestimation of RGC using the automated method.

Whole Retinal Analysis and Retinal Isodensity Map Generation

The program has the integrated ability to efficiently provide whole-retinal RGC quantification and generate a corresponding retinal isodensity map (“heat map”; Fig. 7). The script is able to automatically delineate the retinal wholemount borders and is able to exclude small areas of artifact. Retinal wholemount

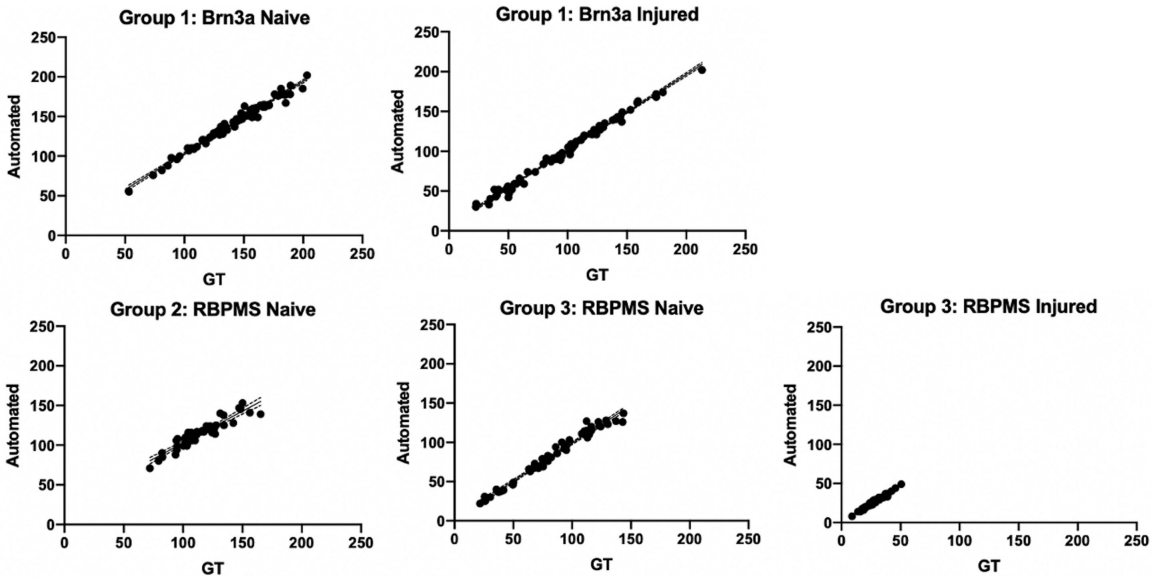

Figure 6. Linear regression analysis in naïve and injured retina demonstrated a strong linear correlation between the averaged manual counts of three observers (Ground Truth [GT]) and automated cell counts. Group 1, Brn3a OHT model ($n = 80$ frames for both naïve and injured retinas); group 2, RBPMS naïve cohort ($n = 48$ frames for naïve retinas only); group 3, RBPMS NMDA model ($n = 48$ frames for both naïve and injured retinas).

Table 4. Reported Automated Methods for RGC Counting in the Rodent Retina

Author	Immunostain	Free to use?	Accuracy
Guymer et.al. (2020)	Brn3a	Yes	
	- Naïve retina		R2 = 0.979
	- Injured retina		R2 = 0.991
	RBPMS		
	- Naïve retina		R2 = 0.875 – 0.979
	- Injured retina		R2 = 0.978
Nadal Nicholás et al. (2009)[15]	Brn3a	No	R2 = 0.98
Geeraerts et al. (2016)[16]	Brn3a	Yes	R2 = 0.96 (widefield images) R2 = 0.99 (confocal images)
Salinas-Navarro et al. (2009)[21]	Fluorogold	No	R2 = 0.99
Denias et al. (2002)[17]	Fluorogold	Yes	R2 = 0.94
Danias et al. (2003)[10]	Fluorogold	Yes	R2 = 0.95
Dordea et al. (2016)[30]	DAPI and βIII Tubulin	Yes	R2 = 0.64 (optimal quality images) R2 = 0.22 (poorer quality images)

RGC automated counts are displayed in a summary table, which can be exported into an Excel (Microsoft Office) spreadsheet, and the counted image with corresponding heat map can be saved as a high-resolution JPEG or PNG file. Retinal wholemount RGC automated counts can be visually checked against the original immunolabeled image by zooming in on any area of interest. The density of cells across the image is calculated using a Kernal Density Estimate (KDE) to generate the heat map. Please refer to Supplementary Material S1 (Heat Map Generation section) for a more detailed explanation.

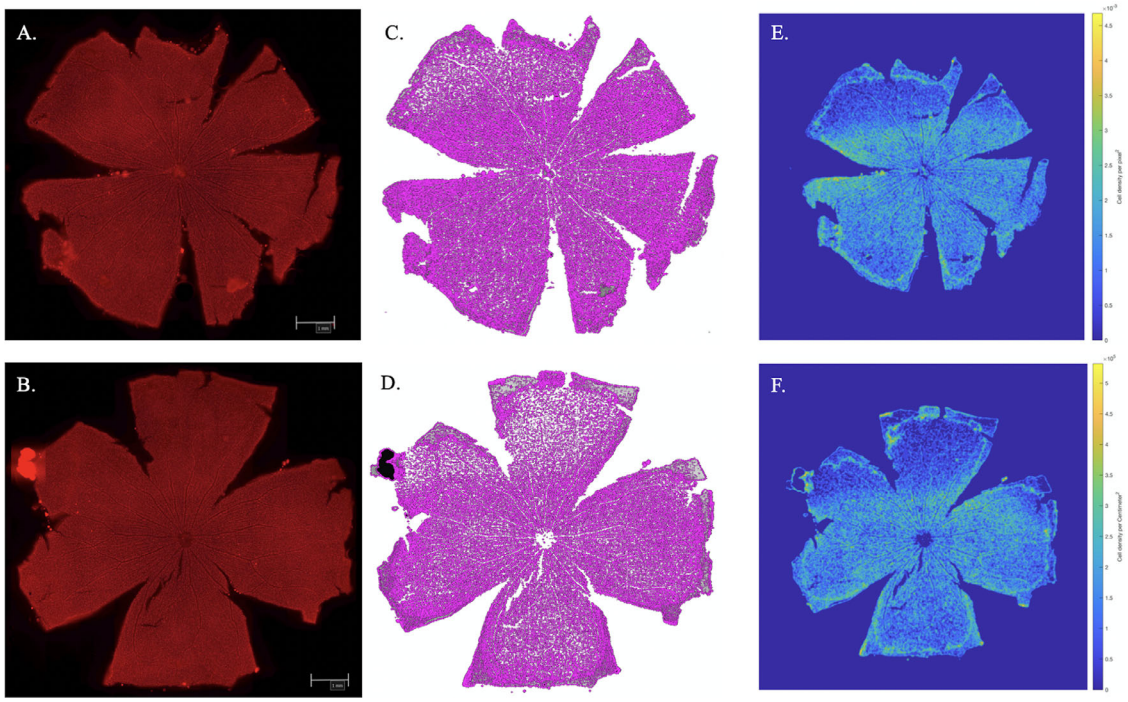

Figure 7. Representative images of (A, B) original image of two naïve retinal wholemounts immunolabeled with Brn3a (captured on Hamamatsu NanoZoomer 2.0-HT fluorescence module, 20 × magnification, viewed using the Hamamatsu NanoZoomer Digital Pathology system, exported as a TIFF), (C, D) respective whole-retinal RGC quantification and (E, F) corresponding retinal isodensity maps ("heat maps"). Scale bar = 1 mm.

Discussion

Manual counting has traditionally represented the standard way to accurately quantify RGC populations on immunohistochemically labeled retinal wholemounts. This procedure, however, is a labor intensive and time-consuming task prone to subjectivity relating to sampling bias and inter/intra-observer variability. This, in turn, has motivated us to develop software built on the MathWorks product to perform automated cell counts. Our program, which we intend to make freely available, has the versatility of being able to analyze RGC-specific labels (Brn3a and RBPMS) and can handle both naïve and diseased retinas. We have validated this software against the manual counting of three independent observers and proven that it possesses an accuracy is at least comparable to quoted data in the recent literature[10,15–17,29,30] (Table 4). We have also demonstrated this script's ability to provide efficient automated RGC counts of entire retinal wholemounts, permitting the generation of retinal isodensity maps to allow the detection of regional differences in RGC density. These features have been seamlessly integrated into the script, thereby avoiding use of commercially available software packages.

The only limiting "human factor" in quantifying cells with our software is the definition of the critical objective parameters, such as pixel diameter based on cell size and percentage fill within each circular rim, color channel, and histogram thresholds. Once calibrated to ensure adequate cell capture for each respective label, then an automated batch analysis of a series of images can be efficiently performed. Although there may be a slight over- or under-representation of true RGC counts, automated cell counting using fixed objective parameters is more likely to generate consistent RGC counts upon repeated sampling than using a manual method with considerable potential subjectivity, and, therefore, variability.[31]

Our program provides a useful research tool with a number of attractive features: (1) wide spectrum of automation, including both image optimization and RGC quantification; (2) applicability to a variety of different antigens (validated to date for the RGC-specific labels Brn3a and RBPMS) with accuracy comparable to manual counting and the existing literature; (3) interchangeability in handling both naive and injured retinal wholemounts; (4) ability to differentiate clusters or clumps of cells with acceptable accuracy; (5) "batch processing" function with seamless transfer of tabulated results to a spread sheet application for

ease of statistical analysis; and (6) automated whole-retinal analysis with integrated retinal isodensity map generation.

In addition to these features, our software also provides the ability to manually adjust and optimize cell capture for weaker cell labeling by changing histogram parameters, cell size, percentage fill, cell intensity, and adaptive thresholding. Moreover, the accuracy of cell detection can be manually checked by the "link zoom" feature, which enables the user to zoom in on sections to check that exclusion parameters are as accurate as possible.

Comparison of our Novel Software to Existing Automated Counting Software

Danias et al.[10,17] were arguably the first to conceive and validate a freely available software called ImageTool to provide semi-automated counts of Fluorogold labeled RGCs on rat, and then later mouse, retinal wholemounts. This software, however, requires time-intensive preprocessing steps using separate software (Adobe Photoshop, Adobe Systems, Inc., San Jose, CA) for images prior to generating the automated cell counts.[17] Image preprocessing is integrated into the script of our software, provided that the actual immunolabeling and resultant image capture are of reasonable quality.

The Vidal-Sanz laboratory also developed a script validated for Fluorogold-labeled RGCs on rodent retinal flat mounts and this was later validated for Brn3a-labeling with excellent accuracy ($R2 > 0.94$) when compared to manual counting.[4,15,29] In addition, they also validated its use in quantifying immunolabeled photoreceptors.[32] Importantly, this program is also able to distinguish between clusters of cells and automates the image optimization stages. From a mosaic of 154 frames of the retinal whole-mount photographs, retinal isodensity maps were generated using Adobe Photoshop CS 8.0.1 (Adobe Systems, Inc.), IPP (IPP version 5.1 for Windows; Media Cybernetics, Silver Spring, MD), and Sigmaplot (Sigmaplot version 9.0 for Windows; Systat Software, Inc., Richmond, CA) commercial software.[29] The only potential disadvantage to its widespread use is that it requires the commercially available software Image Pro-Plus. Geeraerts et al.[16] developed an ImageJ plug-in to provide semi-automated counts of Brn3a-labelled RGCs on mouse retinal wholemounts with excellent accuracy ($r > 0.99$) that permitted the generation of retinal isodensity maps integrated into the script. Manual interventions that are required involve the outlining the borders of the retina and excluding damaged regions / artifacts from the retinal image.[16] We have integrated both whole-retinal analysis and retinal isodensity map generation into our script, which does not require the user to outline the retinal borders. A degree of image optimization is also integrated into our script, to enable the exclusion of small artifacts ("speckles") and background blur. Heavily damaged regions or large artifacts, however, do need to be removed prior.

To our knowledge, Dordea et al.[30] were the first to validate automated RGC counts for Beta-III tubulin and DAPI-labeled RGCs with use of a machine-learning plug-in using CellProfiler open source software. It was estimated that data acquisition was accelerated 10-fold by this automated program. This software requires both an image preprocessing step involving binary contrast enhancement carried out through ImageJ software prior to quantification using CellProfiler, and an initial supervised machine-learning step to ensure accuracy in automated cell recognition for each label.[30]

An open source ImageJ plug-in was developed and validated by Hedberg Buenz et al.[33] for quantifying hematoxylin and eosin-labeled mouse retinal whole-mounts ($R2 = 0.953$ to 0.993). RGCs were identifiable with reasonable accuracy (83.2%) by using random forest classification based on morphological criteria.[31] Similar to our program, this plug-in initially requires the user to manually calibrate the program with a "training" set of images to ensure accurate RGC detection prior to performing automated RGC counts. Despite using high magnification (200×) photomicrographs and manually subtracting artifacts from photomicrographs prior to automated counting, some difficulty was encountered with missed nuclei associated with cell clumps or concealment by the nerve fiber layer.[33] Hedberg Buenz et al.[33] also report that the program is cumbersome when used in conjunction with immunohistochemistry or retrograde tracers, thereby limiting its versatility.

Byun et al.[34] also developed an ImageJ plug-in for nuclei detection on transverse retinal sections, which to date has not been validated for use on whole-mounts. Last, Bizrah et al.[35] developed a MATLAB script to automatically quantify apoptotic RGCs in vivo using fluorescent Annexin V labeling with Detection of Apoptosing Retinal Cell (DARC) imaging ($r = 0.978$, $R2 = 0.956$). This is particularly attractive as the ability to capture and automatically quantify RGC populations in real-time throughout disease evolution, ex vivo, could provide further robustness to preclinical, and even clinical, trials whereas significantly reducing required sample sizes with repeated sampling, accelerating workflow and research output.

Challenges to Counting RGCs

Indistinct cells: Over- or underestimation of RGC counts can potentially lead to erroneous conclusions in animal models of retinal pathology. Our program fundamentally works by separating the cell image from the background image (see Supplementary Fig. S1: Algorithm Development, steps 1–3). By calculating and then removing the background blur, even the faintest cells are observable. When calibrating the program prior to analyzing each immunolabel, the researcher is able to correct for over- or underestimation of RGCs by adjusting the objective parameters and then proceeding to "batch" analyze their image data set.

Our program is able to discriminate cells in clusters with excellent accuracy for Brn3a and RBPMS immunolabels. This is achieved through highlighting the intensity of the boundaries between cells by ensuring the processed image channel intensity occupies the complete intensity range. However, there is still a small window of sampling error whereby a larger cell may be incorrectly counted as two or more separate cells, or vice versa.

Sampling bias: Unless the entire retina is analyzed for RGC quantification, sampling error can arise. RGC density in the rat retina ranges according to location, with the highest density peaking in the most central area (~3000 cells per mm^2) and lowest in the peripheral retina (~600 cells per mm^2).[36] However, the spatial distribution of RGCs can vary between rats of the same species and between eyes of the same rat.[17] There may also be sectoral RGC loss in different disease models.[14,37] Therefore, although it is scientifically acceptable to quantify RGCs in predefined areas sampled at a set distance from the optic nerve in hemiretinas or quadrants,[14] this method ultimately accepts that there is variability compared with counting all cells in the retina. Sampling the entire retina is arduous unless automated counting is utilized to expedite the process. Our automated cell counting program can be used to quantify RGCs in the entire retina to permit isodensity map generation and avoid possible sampling bias.

Image quality: Although various preprocessing techniques can be used to fine-tune poorer quality images, optimal image capture is the prerequisite for accurate quantification of any cellular label. Our software has inbuilt image preprocessing capability to remove artifact and background noise and sharpen image quality. It does, however, require images to be homogenously labeled, be reasonably clean without significant large debris obscuring cells, and to be well focused in a single plane. These are obviously technical issues that should be addressed prior to attempting automated quantification of cells with any software, or even manual counting.

Conclusions

Quantifying immunostained RGCs on wholemounts remain an important outcome measure in preclinical animal studies. Manual or semi-automated methods are labor-intensive, time-consuming, and subject to inter- and intra-observer variability. Our automated cell counting software, validated for the RGC specific immunostains Brn3a and RBPMS in rodent retinal wholemounts, accelerates data acquisition and reduces analytical subjectivity. Our automated software demonstrated accuracy and reproducibility in both naïve and injured retinas when compared with manual counting and has the ability to perform whole-retinal analysis with integrated retinal isodensity map generation.

Acknowledgments

Supported by the National Health and Medical Research Council (APP1102568). The funding source had no role in the design and conduct of this study; collection, management, analysis, and interpretation of data; preparation, review, or approval of the manuscript; and decision to submit the manuscript for publication.

Disclosure: **C. Guymer**, None; **L. Damp**, None; **G. Chidlow**, None; **J. Wood**, None; **Y.F. Tang**, None; **R. Casson**, None

References

1. Casson RJ, Chidlow G, Wood JP, Crowston JG, Goldberg I. Definition of glaucoma: clinical and experimental concepts. *Clin Experiment Ophthalmol*. 2012;40:341–349.
2. Peinado-Ramon P, Salvador M, Villegas-Pérez MP, Vidal-Sanz M. Effects of axotomy and intraocular administration of NT-4, NT-3, and brain derived neurotrophic factor on the survival of adult rat retinal ganglion cells: a quantitative in vivo study. *IOVS*. 1996;37:489–500.
3. Thanos S. Specific transcellular carbocyanine-labelling of rat retinal microglia during

injury-induced neuronal degeneration. *Neurosci Lett*. 1991;127:108–112.
4. Nadal-Nicolás FM, Jiménez-López M, Salinas-Navarro M, et al. Whole number, distribution and co-expression of Brn3 transcription factors in retinal ganglion cells of adult albino and pigmented rats. Harvey AR, ed. *PLoS One*. 2012;7:1–16.
5. Kwong JMK, Quan A, Kyung H, Piri N, Caprioli J. Quantitative analysis of retinal ganglion cell survival with RBPMS immunolabeling in animal models of optic neuropathies. *Investig Opthalmology Vis Sci*. 2011;52:9694–9702.
6. Rodriguez AR, de Sevilla Müller LP, Brecha NC. The RNA binding protein RBPMS is a selective marker of ganglion cells in the mammalian retina. *J Comp Neurol*. 2014;522:1411–1443.
7. Surgucheva I, Weisman AD, Goldberg JL, Shnyra A, Surguchov A. γ-Synuclein as a marker of retinal ganglion cells. *Mol Vis*. 2008;14:1540–1548.
8. Jiang S-M, Zeng L-P, Zeng J-H, Tang L, Chen X-M, Wei X. β-III-Tubulin: a reliable marker for retinal ganglion cell labeling in experimental models of glaucoma. *Int J Ophthalmol*. 2015;8:643–652.
9. Thanos S. The relationship of microglial cells to dying neurons during natural neuronal cell death and axotomy-induced degeneration of the rat retina. *Eur J Neurosci*. 1991;3:1189–1207.
10. Danias J, Lee KC, Zamora M-F, et al. Quantitative analysis of retinal ganglion cell (RGC) loss in aging DBA/2NNia glaucomatous mice: comparison with RGC loss in aging C57/BL6 mice. *Investig Opthalmology Vis Sci*. 2003;44:5151–5162.
11. Buckingham BP, Inman DM, Lambert W, et al. Progressive ganglion cell degeneration precedes neuronal loss in a mouse model of glaucoma. *Neurobiol Dis*. 2008;28:2735–2744.
12. Chen H, Wei X, Cho K-S, et al. Optic neuropathy due to microbead-induced elevated intraocular pressure in the mouse. *Investig Opthalmology Vis Sci*. 2011;52:36–44.
13. Schlamp CL, Montgomery AD, Mac Nair CE, Schluart C, Willmer DJ, Nickells RW. Evaluation of the percentage of ganglion cells in the ganglion cell layer of the rodent retina. *Mol Vis*. 2013;19:1387–1396.
14. Mead B, Thompson A, Scheven BA, Logan A, Berry M, Leadbeater W. Comparative evaluation of methods for estimating retinal ganglion cell loss in retinal sections and wholemounts. Badea TC, ed. *PLoS One*. 2014;9:1–9.
15. Nadal-Nicola´s FM, Jiménez-López M, Sobrado-Calvo P, et al. Brn3a as a marker of retinal ganglion cells: qualitative and quantitative time course studies in naïve and optic nerve–injured retinas. *Investig Opthalmology Vis Sci*. 2009;50:3860–3868.
16. Geeraerts E, Dekeyster E, Gaublomme D, Salinas-Navarro M, De Groef L, Moons L. A freely available semi-automated method for quantifying retinal ganglion cells in entire retinal flatmounts. *Exp Eye Res*. 2016;147:105–113.
17. Danias J, Shen F, Goldblum D, et al. Cytocarchitecture of the retinal ganglion cells in the rat. *Invest Ophthalmol Vis Sci*. 2002;43:587–594.
18. Markand S, Saul A, Roon P, et al. Retinal ganglion cell loss and mild vasculopathy in methylene tetrahydrofolate reductase (Mthfr)-deficient mice: a model of mild hyperhomocysteinemia. *Investig Opthalmology Vis Sci*. 2015;56:2684–2695.
19. Inman DM, Lambert WS, Calkins DJ, Horner PJ. α-Lipoic acid antioxidant treatment limits glaucoma-related retinal ganglion cell death and dysfunction. Ohlmann A, ed. *PLoS One*. 2013;8:1–17.
20. Soto I, Oglesby E, Buckingham BP, et al. Retinal ganglion cells downregulate gene expression and lose their axons within the optic nerve head in a mouse glaucoma model. *J Neurosci*. 2008;28:548–561.
21. Salinas-Navarro M, Jiménez-López M, Valiente-Soriano FJ, et al. Retinal ganglion cell population in adult albino and pigmented mice: a computerized analysis of the entire population and its spatial distribution. *Vision Res*. 2009;49:637–647.
22. Levkovitch-Verbin H, Quigley HA, Martin KRG, Valenta D, Baumrind LA, Pease ME. Translimbal laser photocoagulation to the trabecular meshwork as a model of glaucoma in rats. *Investig Opthalmol Vis Sci*. 2002;43:402–410.
23. Ebneter A, Chidlow G, Wood JPM, Casson RJ. Protection of retinal ganglion cells and the optic nerve during short-term hyperglycemia in experimental glaucoma. *Arch Ophthalmol*. 2011;129:1337–1344.
24. Ebneter A, Casson RJ, Wood JPM, Childow G. Microglial activation in the visual pathway in experimental glaucoma: Spatiotemporal characterization and correlation with axonal injury. *Investig Ophthalmol Vis Sci*. 2010;51:6448–6460.
25. Bull ND, Chidlow G, Wood JPM, Martin KR, Casson RJ. The mechanism of axonal degeneration after perikaryal excitotoxic injury to the retina. *Exp Neurol*. 2012;236:34–45.
26. Chidlow G, Wood JPM, Casson RJ, et al. Expression of inducible heat shock proteins Hsp27 and Hsp70 in the visual pathway of rats subjected to various models of retinal ganglion cell injury. Agudo-Barriuso M, ed. *PLoS One*. 2014;9:1–26.

27. Parker RA, Weir CJ, Rubio N, et al. Application of mixed effects limits of agreement in the presence of multiple sources of variability: exemplar from the comparison of several devices to measure respiratory rate in COPD patients. *PLoS One*. 2016;11:1–15.
28. Bland JM, Altman DG. Agreement between methods of measurement with multiple observations per individual. *J Biopharm Stat*. 2007;17:571–582.
29. Salinas-Navarro M, Mayor-Torroglosa S, Jiménez-López M, et al. A computerized analysis of the entire retinal ganglion cell population and its spatial distribution in adult rats. *Vision Res*. 2009;49:115–126.
30. Dordea AC, Bray M-A, Allen K, et al. An open-source computational tool to automatically quantify immunolabeled retinal ganglion cells. *Exp Eye Res*. 2016;147:50–56.
31. Hedberg-Buenz A, Christopher MA, Lewis CJ, et al. Quantitative measurement of retinal ganglion cell populations via histology-based random forest classification. *Exp Eye Res*. 2016;146:370–385.
32. Ortín-Martínez A, Jiménez-López M, Nadal-Nicolás FM, et al. Automated quantification and topographical distribution of the whole population of S- and L-cones in adult albino and pigmented rats. *Investig Opthalmology Vis Sci*. 2010;51:3171–3183.
33. Hedberg-Buenz A, Christopher MA, Lewis CJ, et al. RetFM-J, an ImageJ-based module for automated counting and quantifying features of nuclei in retinal whole-mounts. *Exp Eye Res*. 2016;146:386–392.
34. Byun J, Verardo MR, Sumengen B, Lewis GP, Manjunath BS, Fisher SK. Automated tool for the detection of cell nuclei in digital microscopic images: application to retinal images. *Mol Vis*. 2006;12:949–960.
35. Bizrah M, Dakin SC, Guo L, et al. A semi-automated technique for labeling and counting of apoptosing retinal cells. *BMC Bioinformatics*. 2014;15:169.
36. Sefton AJ, Dreher B, Harvey AR, Martin PR. *The Rat Nervous System*. Fourth Edi. (Paxinos G, Ed.). Elsevier Inc.; 2015.
37. Lei Y, Garrahan N, Hermann B, et al. Topography of neuron loss in the retinal ganglion cell layer in human glaucoma. *Br J Ophthalmol*. 2009;93:1676–1679.